Icarus 213 (2011) 24–42

Contents lists available at ScienceDirect

Icarus

journal homepage: www.elsevier.com/locate/icarus

# Protocore destabilization in planetary embryos formed by cold accretion: Feedbacks from non-Newtonian rheology and energy dissipation

Ja-Ren Lin [a,b,*], Taras V. Gerya [b], Paul J. Tackley [b], David A. Yuen [c], Gregor J. Golabek [b]

[a] Institute of Oceanography, National Taiwan University, Taiwan
[b] Geophysical Fluid Dynamics Group, Institute of Geophysics, Department of Geosciences, ETH-Zurich, Switzerland
[c] University of Minnesota Supercomputing Institute and Department of Geology and Geophysics, University of Minnesota, Minneapolis, USA

ARTICLE INFO

*Article history:*
Received 10 October 2010
Revised 12 February 2011
Accepted 21 February 2011
Available online 4 March 2011

*Keywords:*
Planetary formation
Thermal histories
Interiors

ABSTRACT

It is suggested that a distinct population of Mars-sized planetary embryos can form by cold accretion in the outer part of the terrestrial zone. A possible radial structure for such embryos consists of an outer silicate-rich layer and an undifferentiated solid protocore. The protocore is divided in a cold undifferentiated central region, a layer of iron, and an outer shell of undifferentiated material. This structure is gravitationally unstable. We investigate the influence of the rheology of the silicate-rich material and of the thermal effects on the protocore destabilization and on the iron core formation. We use a 2D thermomechanical numerical model of a self-gravitating planetary body. The planetary surface is treated as a free surface by imposing a massless weak medium. Our calculations include a non-Newtonian temperature-, pressure-, and strain rate-dependent viscoplastic rheology and thermal contributions from shear heating. We explored the influence of rheology by varying the activation volume, friction angle, and the maximum yield strength of silicate-rich layers. We distinguished three different core formation regimes: exposure mode, fragmentation mode, and transition mode. Like in previous models with Newtonian rheology, the core experiences large deviations from the spherical shape and is temporarily exposed at the surface in the exposure mode. In contrast to the Newtonian models the destruction of the protocores in the fragmentation modes is driven by (i) the spontaneous strain localization along planetary-scale shear zones forming inside the protocore, and/or (ii) descending localized iron diapirs/sheets penetrating the protocore. Feedback from energy dissipation notably modifies the thermal structure of the deforming planetary body. In particular it causes a temperature increase of up to several hundred Kelvin (i) around the moving and deforming protocore and (ii) along planetary scale rupture zones that form inside the protocore. If the protocore is large and has a high viscosity, a large fraction of the dissipated heat is used to increase the temperature of iron.



## 1. Introduction

The core formation of the terrestrial bodies is one of the most important events during the early history of the Solar System. Various mechanisms have been suggested for core formation, but no consensus is reached so far. The iron cores of the terrestrial planets likely form via different processes that take place over an extended period of time and may partly overlap. The dominant process depends on the thermal state of the planetary body (Stevenson, 1990; Rubie et al., 2007), and is thus closely related to the accretion history.

Due to the decay of short-lived radioactive isotopes such as $^{26}$Al and $^{60}$Fe, core formation could occur at a very early stage of the Solar System via the rainfall mechanism (Baker et al., 2005). In this model, molten iron droplets sink towards the bottom of a molten silicate magma ocean because of their higher density. Evidence from meteorites and thermal models support partial, or even large-scale melting processes on small bodies (Greenwood et al., 2005; Hevey and Sanders, 2006; Sahijpal et al., 2007; Day et al., 2009). As a result, planetary embryos may be accreted from predifferentiated bodies. However, if small bodies accreted later, the melting and differentiation may not happen because of insufficient radiogenic heating. Planetary embryos could accrete and remain for several Myr in the outer region of the terrestrial zone, which corresponds to the present asteroid belt (Chambers and Wetherill, 1998, 2001; Wetherill, 1992; O'Brien et al., 2007) before being ejected from that region and possibly contributing to the growth of the final terrestrial planets. These bodies could have a longer

* Corresponding author at: Institute of Oceanography, National Taiwan University, No. 1, Sec. 4, Roosevelt Rd., Taipei 10617, Taiwan.
*E-mail addresses:* linj@erdw.ethz.ch (J.-R. Lin), taras.gerya@erdw.ethz.ch (T.V. Gerya), ptackley@ethz.ch (P.J. Tackley), daveyuen@gmail.com (D.A. Yuen), gregor.golabek@erdw.ethz.ch (G.J. Golabek).

0019-1035/$ - see front matter © 2011 Elsevier Inc. All rights reserved.
doi:10.1016/j.icarus.2011.02.021

accretion time and form cold as the accretion rate is dependent on the radial distance from the Sun (Grimm and McSween, 1993). Core formation on such bodies could be delayed as no impact-induced runaway differentiation can occur on these cold bodies (Ricard et al., 2009). As the average size of accreted bodies increases with time (Wetherill, 1992), the impacts become energetic enough to induce significant melting near the surface when the planetary embryo reaches the mass of Mars (Melosh, 1990). This cold accretion scenario, which neglects the short-lived radioactive heating has been studied for Mars- and Earth-sized planetary bodies (Sasaki and Nakazawa, 1986; Honda et al., 1993; Karato and Murthy, 1997; Senshu et al., 2002). These models suggest a three-layer structure inside the planetary body. The outermost shell is mainly composed of molten silicates as the iron–silicate differentiation can take place in impact-induced magma oceans. As a result of iron–silicate separation in this layer, a dense iron layer can form at the bottom of the magma ocean. The innermost region is still cold and consisted of undifferentiated chondritic material (iron + silicates).

The dense iron layer located on top of the undifferentiated material is gravitationally unstable. This configuration can be examined via Rayleigh–Taylor instability analysis. Ida et al. (1987) and Zhong et al. (2000) investigated analytically the instability of an iron layer in 2D spherical/cylindrical geometry including global degree 1 instability. The mode (in the Rayleigh–Taylor instability) of core formation is influenced by the thermal state of the central region of the planetary embryo. Short-wavelength (degree $L \geqslant 2$ modes) mechanisms producing kilometer-sized iron diapirs that sink through the viscous mantle (Elsasser, 1963; Karato and Murthy, 1997; Golabek et al., 2008; Samuel and Tackley, 2008) prefer a higher-temperature of the planetary interior, which sustains a lower viscosity of this region. However, in the scenario of cold accretion, a low temperature and highly viscous protocore forms, and this cold protocore may be destabilized and destroyed through $L = 1$ mode instability of the iron shell (Stevenson, 1981; Ida et al., 1987).

Honda et al. (1993) and Lin et al. (2009) investigated this cold accretion scenario by using numerical models of Newtonian flow in a self-gravitating three-layered fluid sphere consisting of an outermost silicate layer, an iron-rich shell, and the central undifferentiated protocore. Their results confirmed that the actual core formation mechanism is dependent on the viscosity of the protocore and indicated that the mode of core formation could change from lower ($L = 1$) to higher degree ($L \geqslant 2$) mode during the process. In addition, Lin et al. (2009) showed that the duration of core formation correlates with protocore viscosity and predicted that a transient exposure of the protocore towards the planetary surface may occur during core formation. These studies, however, did not address the role played by gravitational energy dissipation during the destabilization of the protocore, and by rheological parameters (including thermal-, strain rate-, and pressure-dependent rheology and brittle/plastic deformation). These ingredients may have strong thermomechanical feedbacks on the core formation process (Golabek et al., 2009).

Senshu et al. (2002) studied the thermal evolution of a growing planetary embryo assuming a cold accretion scenario. They suggest an iron layer formed inside the undifferentiated protocore at the last stage of accretion. Due to the limitations of 1D model setup used by Senshu et al. (2002) it was not possible to treat core formation by degree 1 instability of the iron layer (Stevenson, 1981; Ida et al., 1987, 1989; Honda et al., 1993; Lin et al., 2009). Therefore our study elaborates on the results of Senshu et al. (2002) and performs numerical experiments of a self-gravitating Mars-sized planetary embryo to investigate the unstable iron shell scenario using a realistic temperature-, pressure- and strain rate-dependent rheology, and accounting for the dissipation of gravitational energy.

## 2. Numerical model

### 2.1. The governing equations

We solved the conservative equations of mass and momentum for an incompressible fluid in 2D-Cartesian geometry. The chemical field is modeled with three different types of material, with distinct densities and viscosities (see model setup). In the Lagrangian frame, the equation of mass conservation is

$$\nabla \cdot \mathbf{u} = 0,, \tag{1}$$

where $\mathbf{u}$ is the velocity. The equation of momentum is given by the Stokes equation,

$$\nabla \cdot \sigma - \nabla P = \rho \nabla \Phi(x, z, t), \tag{2}$$

where $\sigma$ is the deviatoric stress tensor, $P$ the total pressure, $\Phi$ the gravitational potential (which is here varying with time and location due to the rearrangement of mass during the differentiation), and $\rho$ the density. We did not account for the thermal buoyancy because during core formation this contribution is much smaller than the chemical buoyancy (i.e., the density difference between iron and protocore) (Honda et al., 1993). To model self-gravitation, we solved the Poisson equation for the gravitational potential as governing equations.

$$\nabla^2 \Phi = 4K\pi\gamma\rho(x, z, t), \tag{3}$$

where $\gamma$ is the gravitational constant, and $K$ a scaling factor equal to 2/3. This value accounts for the fact that we simulated a 3D spherical gravity field in 2D geometry (Gerya and Yuen, 2007; Lin et al., 2009). The heat conservation equation in Lagrangian frame is

$$\rho(c, t) C_p \left(\frac{DT}{Dt}\right) = -\nabla q + H_s + H_r, \tag{4}$$

where $C_p$ is the isobaric heat capacity, $T$ the temperature, and $H_r$ the radioactive heating rate. The heat flux $\boldsymbol{q}$ is defined as

$$q = -k\nabla T, \tag{5}$$

where $k$ is the thermal conductivity. $H_s$ is the shear heating and is calculated by

$$H_s = \sigma_{ij}\dot{\varepsilon}_{ij}. \tag{6}$$

Feedback from this source term is important in our study as it results in the transformation of potential energy into heat, which in turn locally affects the viscosity of rocks. We neglected adiabatic heating/cooling because it has minor effect on Mars-sized bodies in comparison to shear heating (Ichikawa et al., 2010).

The deviatoric strain rate, $\varepsilon_{ij}$, is

$$\dot{\varepsilon}_{ij} = \frac{1}{2}\left(\frac{\partial u_j}{\partial x_i} + \frac{\partial u_i}{\partial x_j}\right), \tag{7}$$

where $u_i$ and $u_j$ are components of the velocity vector $\mathbf{u}$.

In the present study we used a viscoplastic rheology for silicate-rich material. The deviatoric strain rate, $\varepsilon_{ij}$, has two components which derive from the contributions of ductile and brittle/plastic (brittle/plastic yielding) deformation:

$$\dot{\varepsilon}_{ij} = \dot{\varepsilon}_{ij(ductile)} + \dot{\varepsilon}_{ij(brittle)}. \tag{8}$$

The ductile deformation is modeled by

$$\dot{\varepsilon}_{ij(ductile)} = \frac{\sigma_{ij}}{2\eta(T, P, \dot{\varepsilon}, c)}, \tag{9}$$

where $\sigma_{ij}$ is a component of the deviatoric stress from Eq. (2), $\eta(T, P, \dot{\varepsilon}, c)$ is the effective viscosity, which depends on the temperature, pressure, strain rate and composition, and can be defined in terms of the second invariant of the deviatoric strain rate tensor

(Ranalli, 1995). The commonly used effective viscosity for silicate-rich material is:

$$\eta(T,P,\dot{\varepsilon}) = A^{-1/n}(\dot{\varepsilon}_{\mathrm{II}})^{(1-n)/n}\exp\left(\frac{E_a + PV_a}{nRT}\right), \tag{10}$$

where $A$ is the pre-exponential factor, $E_a$ and $V_a$ the activation energy and volume, respectively, $n$ the power law coefficient, $R$ the gas constant, and $\dot{\varepsilon}_{\mathrm{II}} = \left(\frac{1}{2}\dot{\varepsilon}_{ij}\dot{\varepsilon}_{ij}\right)^{1/2}$ the second invariant of the strain rate tensor.

The brittle/plastic deformation can be determined by the second invariant of the deviatoric stress tensor and can be activated when the brittle/plastic yielding criterion is reached.

$$\dot{\varepsilon}_{ij(brittle)} = 0 \quad \text{for } \sigma_{\mathrm{II}} < \sigma_{yield}, \tag{11a}$$

$$\dot{\varepsilon}_{ij(brittle)} = \chi\frac{\partial G}{\partial \sigma_{ij}} = \chi\frac{\sigma_{ij}}{2\sigma_{\mathrm{II}}} \quad \text{for } \sigma_{\mathrm{II}} = \sigma_{yield}, \tag{11b}$$

where $\sigma_{\mathrm{II}} = \left(\frac{1}{2}\sigma_{ij}\sigma_{ij}\right)^{1/2}$ is the second invariant of the deviatoric stress tensor, $G$ the plastic potential of yielding material, $\chi$ plastic multiplier, which can be determined locally at every time step to satisfy the brittle/plastic yielding criterion (Gerya and Yuen, 2007), and $\sigma_{\mathrm{yield}}$ the brittle/plastic yield strength for the given rock. Here, we implement the Mohr–Coulomb yield criterion, which increases linearly with the pressure.

$$\sigma_{yield} = C + \sin(\varphi)P, \tag{12a}$$

where $C$ is the cohesion (residual strength at $P = 0$), and $\varphi$ the effective internal friction angle.

In some experiments, we limited maximal yield strength of silicate-rich materials ($\sigma_{\max}$) by imposing the condition

$$\sigma_{yield} \leqslant \sigma_{\max}, \tag{12b}$$

which is similar to the Peierls stress limit (Kameyama et al., 1999). Eq. (12b) is a simple approximation of the usual Peierls law, with a simplified Peierls stress $\sigma_{\max}$ that is assumed to be independent of temperature and pressure. Plasticity is thus given here by the combination of Mohr–Coulomb (pressure-dependent part) and von Mises (Peierls part) criteria, from which the lowest stress limit is chosen locally.

### 2.2. Numerical method

We used the finite-difference code I2ELVIS (Gerya and Yuen, 2007) to solve the governing equations in 2D-Cartesian geometry. This code implements a Lagrangian marker-in-cell technique for the advection of transport properties in a rectangular staggered Eulerian grid and the so-called "spherical-Cartesian" approach to calculate the dynamics of a deforming cylindrical body on this Cartesian grid (Gerya and Yuen, 2007). In order to calculate the gravitational field for self-gravitation, we solved the Poisson equation and applied a constant gravitational potential as the boundary condition on a circular surface (dashed line in Fig. 1a) (Lin et al., 2009). The cylindrical planetary body is surrounded by a low-viscosity massless medium to simulate an effective free planetary surface. This method is numerically stable and accurate (Gerya and Yuen, 2007; Lin et al., 2009), and it was successfully used in recent

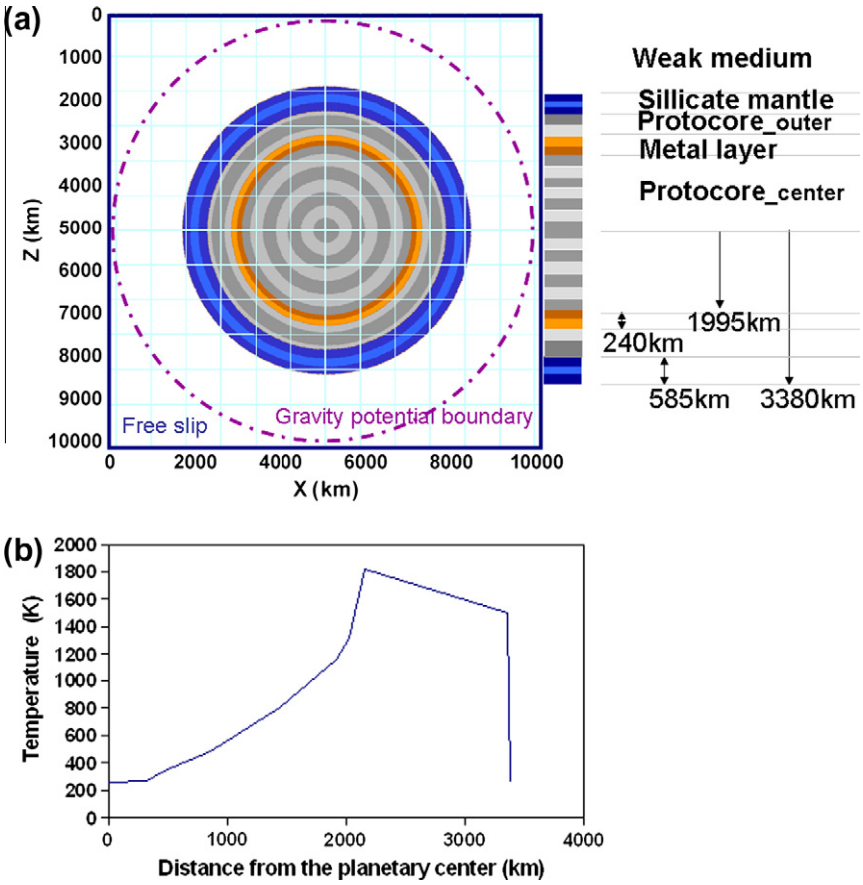


**Fig. 1.** (a) Initial model setup and (b) the initial temperature profile applied in the model. The planetary body in (a) consists of three distinct materials, which are silicates (bright and light blue color, $\rho$ = 3500 kg m$^{-3}$, $d$ = 585 km), metal (dark and light orange color, $\rho$ = 6700 kg m$^{-3}$, $d$ = 240 km), and primitive chondritic material (dark and light gray color, $\rho$ = 3870 kg m$^{-3}$, $R_{\mathrm{inner}}$ = 1995 km). A weak medium (white color, $\rho$ = 1 kg m$^{-3}$) fills the remaining numerical box. A free slip mechanical boundary condition is applied on all boundaries. A constant gravitational potential condition is set on the circular boundary (dashed line). (For interpretation of the references to color in this figure legend, the reader is referred to the web version of this article.)

studies (Schmeling et al., 2008; Lin et al., 2009). Both the distance of the gravitational potential boundary from the planetary surface and the viscosity contrast between the planetary body and the massless medium needed to obtain convergence of the numerical solution have been discussed by Lin et al. (2009).

### 2.3. Model setup

Our initial model setup follows the results of Senshu et al. (2002), who studied the thermal evolution of a growing planetary embryo up to the size of Mars. This study assumes cold accretion, which accounts for the impact heating by relatively small planetesimals, but ignored short-lived radiogenic heating. As a consequence, a hot iron layer formed inside the undifferentiated protocore. Our initial setup is shown in Fig. 1a. The model box is 10,140 km × 10,140 km and the grid resolution is 151 × 151 nodes, with 562,500 markers. The planetary body ($R_p$ = 3380 km) has an undifferentiated protocore and an outer differentiated silicate layer ($d_3$ = 585 km, $\rho_3$ = 3500 kg m$^{-3}$). The protocore consists of an iron layer ($d_2$ = 240 km, $\rho_2$ = 6700 kg m$^{-3}$) located in between an undifferentiated central cold region ($R_{1inner}$ = 1995 km, $\rho_1$ = 3870 kg m$^{-3}$) and a hot undifferentiated shell ($R_{1outer}$ = 2795 km, $\rho_1$ = 3870 kg m$^{-3}$). The subscripts 1–4 stand for the protocore, the iron layer, the silicate layer and the massless medium ($\rho_4$ = 1 kg m$^{-3}$), respectively. We prescribed the temperature profile for a planetary embryo of Senshu et al. (2002) as initial condition (Fig. 1b). This profile was used to calculate the initial viscosity structure of the silicate and protocore layers. The temperature of the massless medium was set to be 273 K for all simulations as we neglected the blanketing effect of the primordial atmosphere surrounding the embryo.

We varied the viscosity of the silicate-rich regions (including protocore and outermost silicate layer) in the range $10^{19}$–$10^{26}$ Pa s, and we fixed the viscosities of both the iron and the massless medium to $10^{19}$ Pa s. However, it should be mentioned that realistic viscosity for iron was suggested to be approximately $10^{-2}$ Pa s in a liquid state (Rubie et al., 2007). Furthermore, the viscosity of silicates may range from 100 Pa s for molten silicates, up to $10^{28}$ Pa s for a cold and solid protocore (Karato and Murthy, 1997). A detailed exploration of these ranges of viscosities is out of reach with our numerical model and may require implementation of multiphase flow physics (e.g., Ricard et al., 2009). We will however estimate the possible effects of iron and massless material viscosities in the discussion.

Given the model setup, the model space to explore is huge. Here, we are focusing on the effects of pressure-dependent rheology and thermal feedbacks from gravitational potential release. We systematically varied activation volume ($V_a$) between 0 and $1.6 \times 10^{-5}$ m$^3$ mol$^{-1}$, and the sine of the internal friction angle ($\sin(\varphi)$) between 0.001 and 0.1. Since the rheology of the chondritic protocore material is not well constrained, we also varied the maximum yield strength of the silicate-rich material, $\sigma_{max}$ from $10^7$ Pa (only the cohesion is important) up to $10^{29}$ Pa (practically, this is equivalent to no limitation for $\sigma_{yield}$, pure viscous behavior). Further physical parameters are given in Table 1.

**Table 1**
Values of physical parameters used in models.

| Symbol | Parameter | Value | Unit |
|---|---|---|---|
| $\Gamma$ | Gravitational constant | $6.67 \times 10^{-11}$ | m$^3$ kg$^{-1}$ s$^{-2}$ |
| $C_p$ | Isobaric heat capacity | 1000 | J kg$^{-1}$ K$^{-1}$ |
| $H_r$ | Radioactive heating | $2.2 \times 10^{-8}$ | W kg$^{-1}$ |
| $A$ | Pre-exponential factor | $5.01 \times 10^{20}$ | Pa$^n$ s |
| $E_a$ | Activation energy | $4.7 \times 10^5$ | J mol$^{-1}$ |
| $V_a$ | Activation volume | 0–$1.6 \times 10^{-5}$ | m$^3$ mol$^{-1}$ |
| $R$ | The gas constant | 8.314 | J K$^{-1}$ mol$^{-1}$ |
| $N$ | The power law coefficient | 4 | |
| $\sigma_{yield}$ | The maximum strength of silicates | $10^7$–$10^{29}$ | Pa |
| $C$ | Cohesion | $10^7$ | Pa |
| $\sin(\varphi)$ | sine of friction angle | 0.01–0.05 | |
| $P_p$ | Radius of the planetary body | 3380 | km |
| $R_{1inner}$ | Radius of inner part of the protocore | 1995 | km |
| $R_{1outer}$ | Radius of outer part of the protocore | 2795 | km |
| $D_2$ | The thickness of the iron layer | 240 | km |
| $D_3$ | The thickness of the silicate layer | 585 | km |
| $P_1$ | The density of the protocore | 3870 | kg m$^{-3}$ |
| $P_2$ | The density of the iron layer | 6700 | kg m$^{-3}$ |
| $P_3$ | The density of the silicate layer | 3500 | kg m$^{-3}$ |
| $P_4$ | The density of the massless medium | 1 | kg m$^{-3}$ |

## 3. Results

To initiate the Rayleigh–Taylor instability, we created a small gravitational perturbation by imposing random distribution of markers. The protocore is driven away from the planetary center in an initial direction that depends on the model. One may point out that this method is a bit ad hoc. It is however a simple way to model the instabilities triggered by impacts on the planetary embryo. The iron starts to accumulate at the planetary center as the protocore keeps its original motion towards the planetary surface and deforms during its motion towards the surface. Note that at this stage, the protoplanet has an aspherical shape. In the final stage, secondary iron drops may form and sink towards the center after the formation of the central iron core. Part of the protocore is surviving after the core formation, but its shape and size may be strongly modified.

### 3.1. Modes of deformation

According to the deformation type of the protocore, we classified all our models into three groups of core formation: The exposure, fragmentation and transition modes (Fig. 2).

Case A (test 93, $\sin(\varphi)$ = 0.04, $V_a = 1.6 \times 10^{-5}$ m$^3$ mol$^{-1}$) (Figs. 2 and 3) illustrates a typical example for the exposure mode of core formation. The protocore is strong, and does not experience deformation until it hits the surface and is exposed. Note the nearly angular shape of the exposed surface, which results from the intense localized shear deformation atop the protocore during its exposure. The exposure of the protocore may only be a transitional episode and be reduced by further deformation inside the proto-

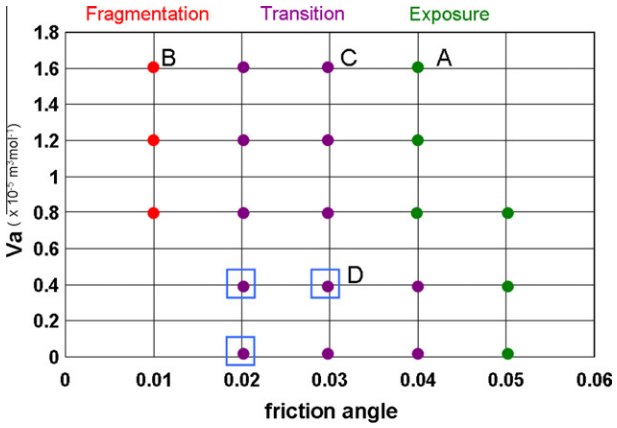


**Fig. 2.** Schematic distribution of core formation modes. Fragmentation mode is shown in red color, exposure mode is given in green, and purple expresses the transition mode. Models with planetary size rupture zones are denoted by a blue square. (For interpretation of the references to color in this figure legend, the reader is referred to the web version of this article.)

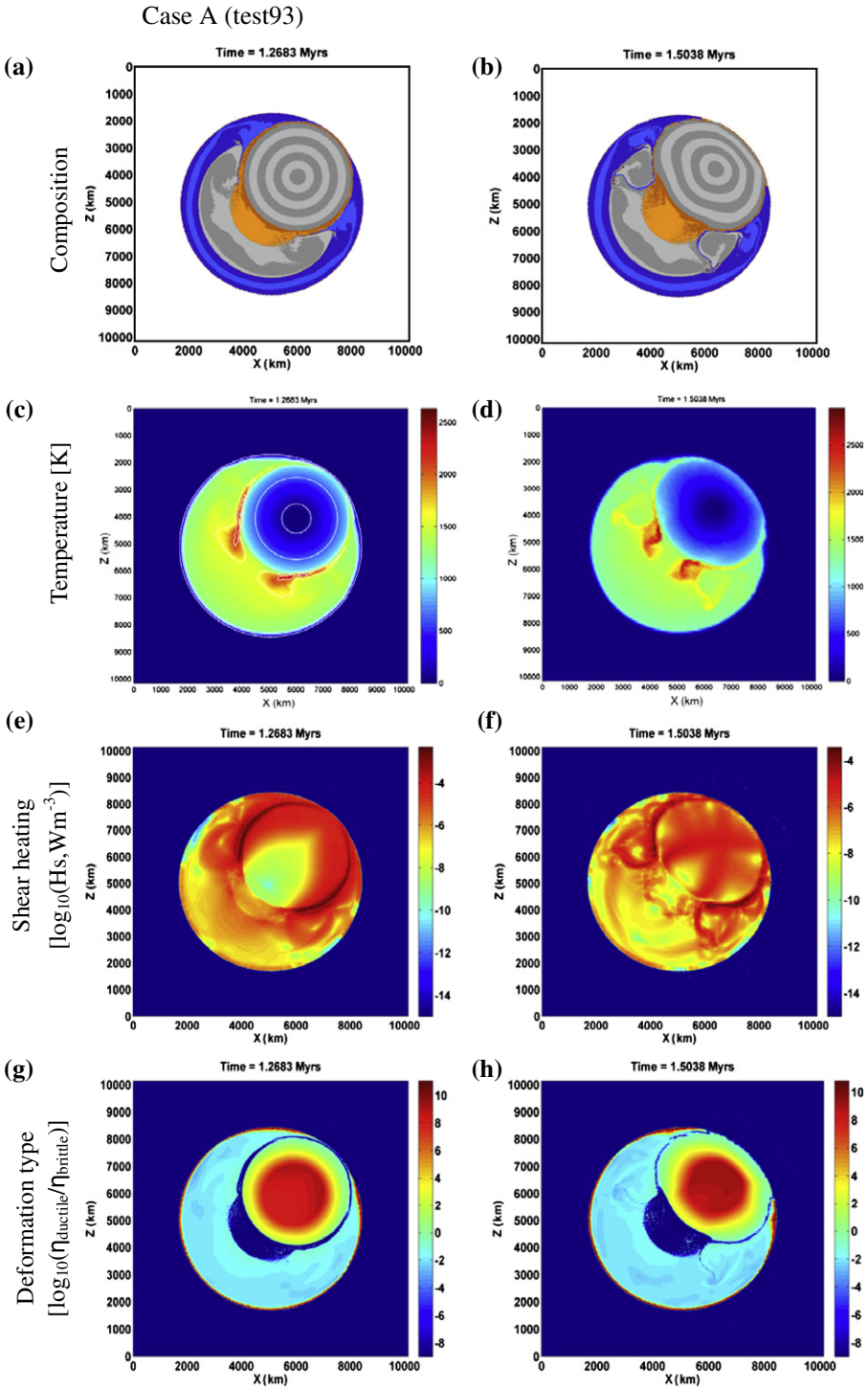


**Fig. 3.** Numerical results characteristic for the exposure mode. From top to bottom we present the chemical, temperature, shear heating, and deformation field from model test 93 for two timesteps each.

core, owing to shear heating. However the rigid protocore can still remain at one side of the newly formed iron core, which has then a non-spherical shape. In Fig. 3b, for instance, the iron core has a half-sphere shape.

Case B (test 64, $\sin(\varphi) = 0.01$, $V_a = 1.6 \times 10^{-5}$ m$^3$ mol$^{-1}$) (Figs. 2 and 4) represents the fragmentation mode, for which no exposure was observed during the core formation. The protocore is too weak to sustain its shape and is deformed by the forming iron core that has created enough deviatoric stress to weaken and yield the protocore. Smaller iron diapirs/sheets forming from the remnants of global iron layer atop the protocore penetrate along the localized zones formed by the protocore yielding process. This mode bears similarity with the model by Stevenson (1981) as the newly formed iron core is surrounded by rockbergs.

Cases C (Figs. 2 and 5), and D (Figs. 2 and 6) both demonstrate the transition mode of core formation. The deformation process of cases C (test 91, $\sin(\varphi) = 0.03$, $V_a = 1.6 \times 10^{-5}$ m$^3$ mol$^{-1}$) and D (test 70, $\sin(\varphi) = 0.03$, $V_a = 4 \times 10^{-6}$ m$^3$ mol$^{-1}$) are closer to the fragmentation mode (e.g., case B). Case C has a tendency to yield due to the deviatoric stress exerted by the iron diapirs. In case D

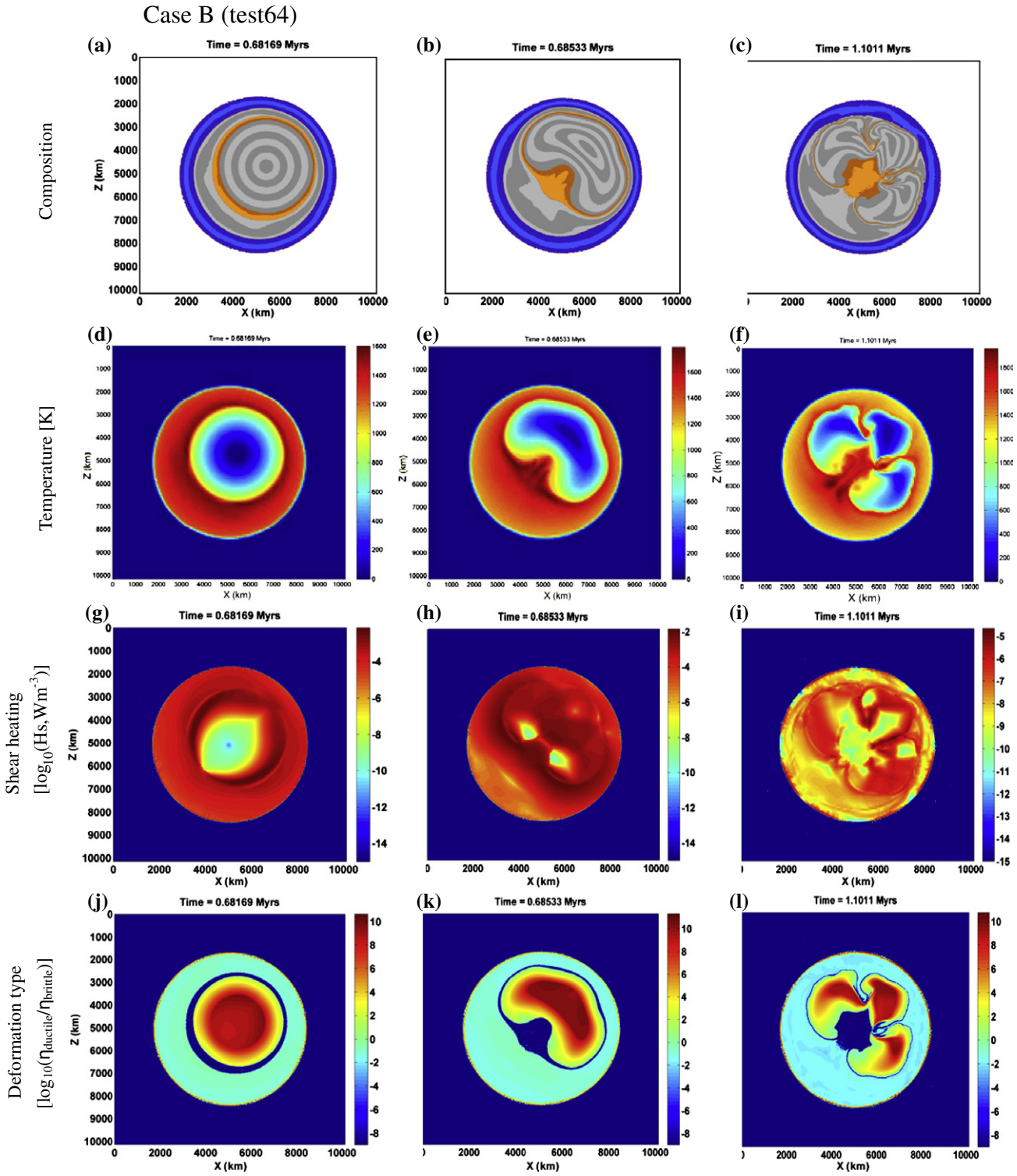


**Fig. 4.** Numerical results for the fragmentation mode. From top to bottom we present the chemical, temperature, shear heating, and the deformation field from model test 64 for three timesteps each.

the iron pond yields the protocore, and two distinct fragments were formed by a rupture zone (Fig. 5). The models characterized by this kind of planetary-scale rupture zones are represented by blue squares in Fig. 2. If the stress release occurs on a short timescale (due, e.g., to thermal runaway processes caused by shear heating), these fractures may cause mega-quakes during core formation.

### 3.2. Influences of physical parameters for model development

#### 3.2.1. Effect of activation volume

The activation volume controls the variations of silicate viscosity with pressure. We varied its value between 0 and $1.6 \times 10^{-5}$ m$^3$ mol$^{-1}$. Fig. 7 displays three cases (each row representing three snapshots of the same case). Clearly, the activation

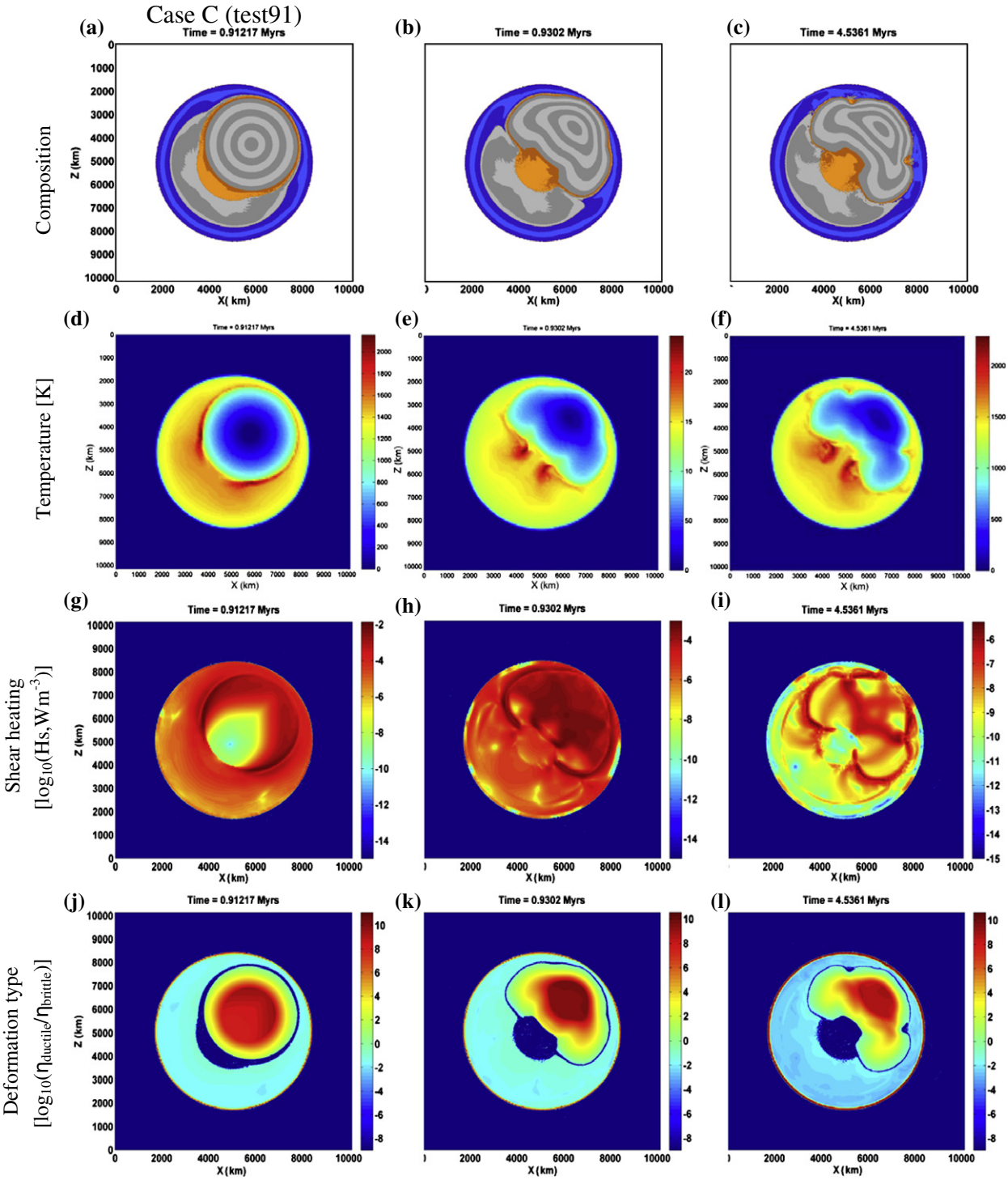


**Fig. 5.** Numerical results for the transition mode. From top to bottom we present the chemical, temperature, shear heating, and deformation field from model test 91 for three timesteps each.

volume has a strong influence on the size and shape of the remaining protocore. In case Test 1, viscosity does not depend on pressure ($V_a = 0$), and is thus mostly sensitive to temperature. The thermal effect is enhanced by the temperature rise due to the shear heating triggered by the motion of the protocore. As a result, the mixing of iron and the material of the outer part of the protocore materials is efficient, and the remaining protocore is small. Interestingly, the mixing between protocore and iron as the protocore translated to the protoplanet's surface was not observed in the experiments with Newtonian rheology (Lin et al., 2009). By contrast, models Test 3 ($V_a = 8 \times 10^{-6}\,\mathrm{m^3\,mol^{-1}}$) and Test 5 ($V_a = 1.6 \times 10^{-5}\,\mathrm{m^3\,mol^{-1}}$) have a large remaining protocore. Furthermore, the shape of this remaining protocore is more spherical in model Test 5 than in model Test 3. The effect of pressure on the viscosity partially balances the effect of temperature. Thus, as the activation volume increases, the viscosity gets large enough to prevent defor-

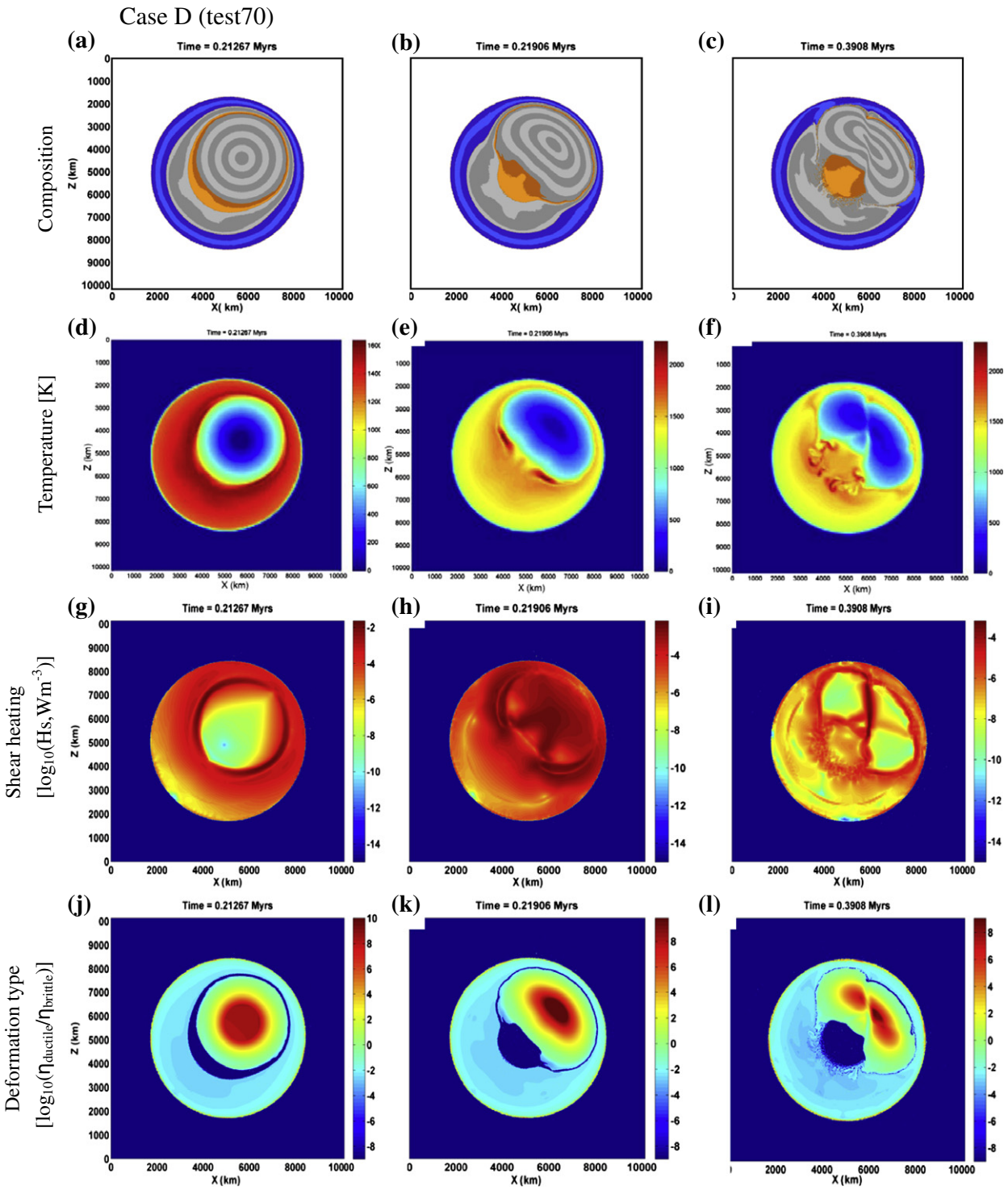


**Fig. 6.** Numerical results for the transition mode. From top to bottom we present the chemical, temperature, shear heating, and deformation field from model test 70 for three timesteps each.

mation and mixing. Overall, this series of experiments suggest that a planetary body with a high activation volume material would have a stronger and longer existing protocore.

### 3.2.2. Effect of the friction angle

The friction angle measures the degree of the yield stress that depends on the confining pressure. The friction angle strongly depends on presence of fluids and melts. For silicate rocks, it varies from about 0.6 in dry conditions, to almost 0 for fluid/melt saturated rock (Ranalli, 1995). Because the volatile-rich, non-differentiated planetary materials are likely fluid/melt saturated, we tested relatively low values of $\sin(\varphi)$. It is important to note that the yield stress strongly increases with the confining pressure when a higher friction angle is used. The influence of the sine of the friction angle is displayed in Fig. 8, with $\sin(\varphi)$ being equal to 0.01, 0.03, and 0.04 from top to bottom. A high friction angle (Test 22) ensures that the protocore keeps its spherical shape until it reaches the planetary surface. By contrast, for low friction angle (Test 10), the protocore

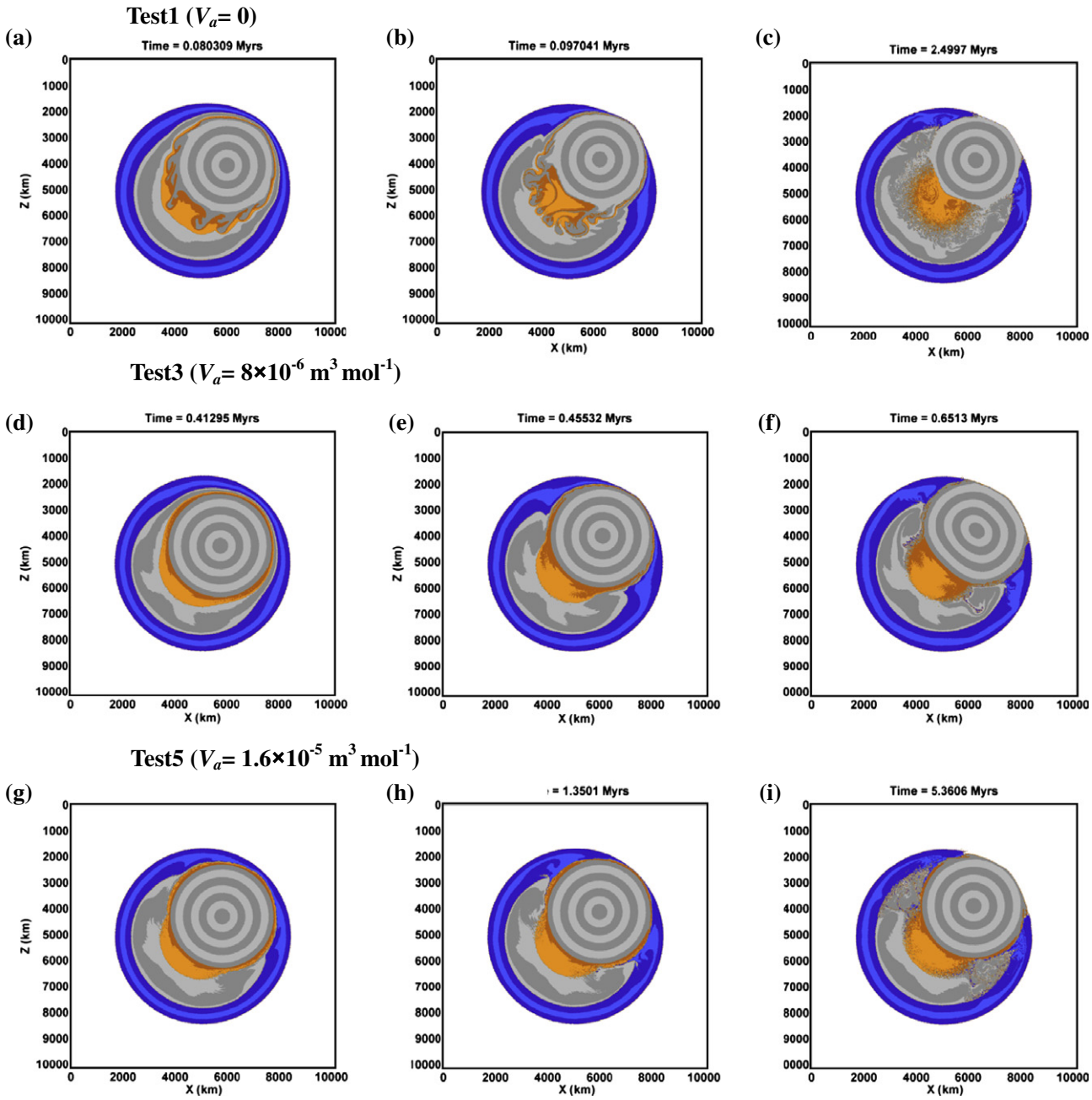


**Fig. 7.** Numerical results from three models (test 1, test 3 and test 5) showing the effect of activation volume on core formation. Three selected figures from each test represent the time evolution shown in one row. From the top to the bottom, the value of the activation volume is increasing.

dislocate in large fragments that surround the newly formed iron core. The yield stress decreases with decreasing friction angle. The protocore becomes thus weaker, is more easily penetrated by accumulated iron ponds, and dislocates into large fragments.

*3.2.3. Effect of the maximal yield strength of the silicate material*

Fig. 9 illustrates the effect of the maximal yield strength of the silicates $\sigma_{max}$. We fixed the values of $\sin(\varphi)$ and $V_a$ to 0.3 and $8.0 \times 10^{-6}$ m$^3$ mol$^{-1}$, which *a priori* correspond to strong a protocore. In Fig. 9, we plotted snapshot of the final stage for models with maximal yield stress equal to (from top to bottom) $3.0 \times 10^7$, $5.0 \times 10^8$, $3.0 \times 10^9$ Pa. As one would expect, the strength of the silicate increases with increasing $\sigma_{max}$. The higher the maximum yield strength, the more rigid the protocore. The protocore can then sustain its shape and be exposed to the surface.

*3.3. Heat partitioning*

*3.3.1. Heat distribution of different deformation modes*

The core formation for the cold accretion scenario restricts the heat production to certain areas. Temperature rise occurred significantly (i) around the moving and deforming protocore, (ii) along planetary scale fracture zones forming in the protocore, and (iii) along passways of iron diapirs/channels penetrating the fragmented protocore (see panels c and d in Fig. 3 and d–f in Figs. 4–6).

Further, we check the average temperature evolution of iron and silicates for four models (first column of Fig. 10). A clear jump of average temperature of iron and silicate can be observed in these models, after which the average temperature of both iron and silicate reaches steady state. These observations about the average temperature are typical for all conducted experiments. In

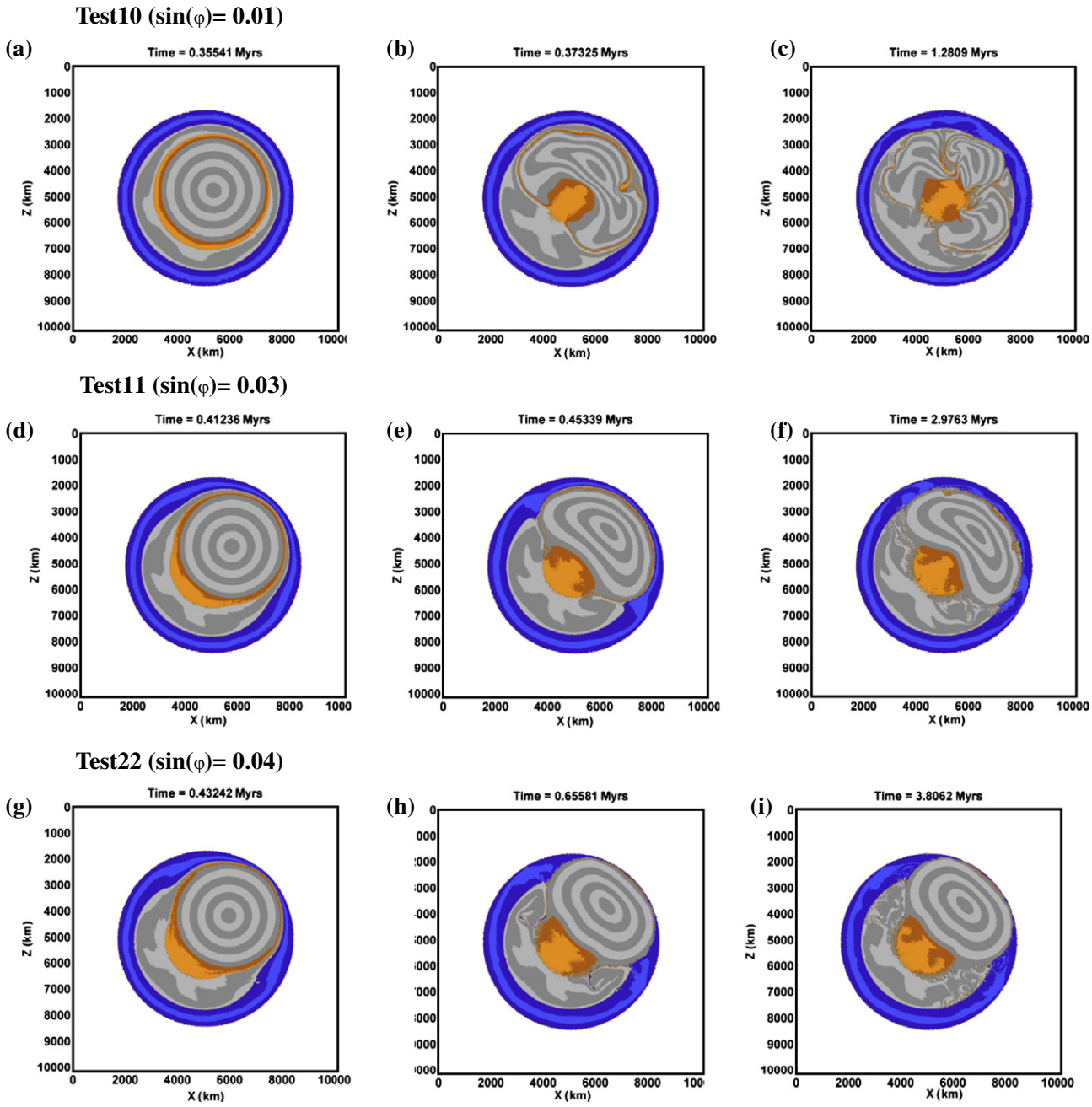


**Fig. 8.** Numerical results from three models (test 10, test 11 and test 22) displaying the effect of the friction angle on core formation. Three selected figures from each test represent time evolution shown in one row. From the top to the bottom, the value of the sine of the friction angle is increasing.

order to compare radial temperature distributions for different models, we plotted these data at four distinct times (Fig. 10): (1) the initial thermal state at 0 Myr (identical for all models), (2) the start and (3) the end of the temperature jump and finally (4) the moment at which steady state in radial temperature distribution is reached. For these four stages we plot radial profiles of the average and standard deviation in density and temperature.

Overall evolution of radial distributions seems to be very similar for all core formation modes. The most dramatic changes in temperature and density distribution occur during a relatively short period of time (corresponding, in our simulations, to time elapsed between instants 2 and 3), during which the iron is entering the planetary center (see second and third column in Fig. 10). This event is accompanied by release of gravitational potential energy that is further transformed into heat (see fourth and fifth column in Fig. 10), thus causing a temperature elevation.

We evaluated the average temperature rise of iron and silicate during this stage for different models. Results are shown in Fig. 11a and b. The average temperature of iron is higher on the upper-right corner of Fig. 11a (large activation volume and friction angle for plastic deformation), which corresponds to models in the exposure mode with a large and rheologically strong protocore. By contrast, the average temperature of silicate is higher in the lower-left corner (small activation volume and friction angle), which corresponds to models with a weak and smaller protocore. The heat partition between iron/silicate can be approximated with $\Delta Q = mC_P\Delta T$, where $\Delta Q$ is heat partition between iron/silicate, $m$ the total mass of iron/silicate, $C_P$ the heat capacity, and $\Delta T$ temperature jump that we

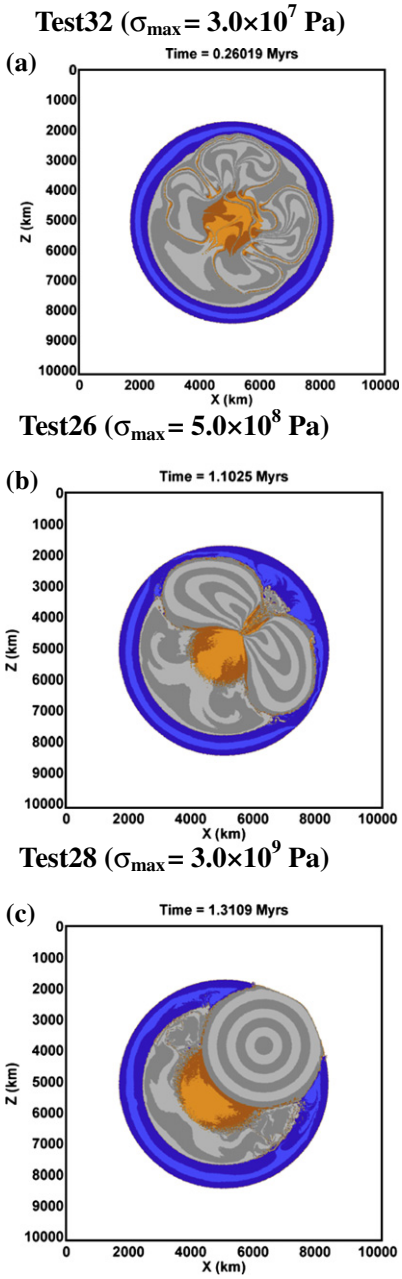


**Fig. 9.** Numerical results from three models (test 32, test 26 and test 28) characterizing the effect of the maximum strength of silicate material on core formation. One snapshot from the final stage of the core formation is shown for each model. From the top to the bottom, the value of the maximum strength is increasing.

observed in models. In our simulations we assumed identical heat capacities for both materials. Fig. 11c plots the ratio of the heat partitioned in iron to the total heat (i.e., the heat on both iron and silicate), without considering heat dissipation to outer space. The ratio of heat partitioned in iron is up to 70%. Again, this value is obtained for a strong protocore rheology (upper-right corner in Fig. 11c), because a stronger protocore can restrict the iron to flow uniformly along its margins, where most of the potential energy is dissipated (see Fig. 3) with less mixing between iron and silicate. On the contrary, more heat can be retained in silicate mantle when more mixing, shear zones (case D), or/and more secondary diapirs/channels (case B) are created in the protocore because more energy is converted to shear heating by the deformation of the silicate mantle (Ke and Solomatov, 2009).

*3.3.2. Effect of shear heating on the deformation modes*

We selected two experiments, test 17($\sin(\varphi) = 0.001$, $V_a = 8 \times 10^{-6}$ m$^3$ mol$^{-1}$) and test 22 ($\sin(\varphi) = 0.04$, $V_a = 8 \times 10^{-6}$ m$^3$ mol$^{-1}$), which represent two end-member modes (the exposure and the fragmentation modes), to perform additional models (test 33 and test 34) that do not account for shear heating feedback. Results are shown in Fig. 12.

Fig. 12a, b, d and e represents snapshots taken at the same equilibrium stage after core formation. The corresponding temperature profiles are plotted in Fig. 12c and f. Interestingly, the reshaping mode does not change when shear heating is switched off. This result may be specific to this cold accretion scenario, because the release of shear heating is limited to localized areas, and the amount of heat is not enough to affect larger regions of the central protocore. However, the average temperature on different radius could be up to 500 K larger when shear heating is accounted for (see Fig. 12c and f).

### 3.4. Aspherical deviation of the planetary embryo

We evaluated the maximum deviation from spherical shape during core formation following the procedure given by Lin et al. (2009). Fig. 11e shows the stretching distance after subtraction of the diameter of the body. The maximum deviation follows the diagonal trend which indicates that the aspherical deviation is controlled by the interplay of activation volume and friction angle. The maximum aspherical deviation (up to 240 km, corresponding to about 3.5% of the diameter) is smaller than the result obtained for Newtonian rheology (up to 360 km, about 5% of the diameter) in our previous study.

To estimate the protocore exposure, we measured the minimum distance of the protocore to the surface (details on the measurement method are described in Lin et al. (2009)). The results are shown in Fig. 11f. We found that the exposure is a function of the applied friction angle. The higher the friction angle, the stronger the rheology, and the larger the exposure of the protocore.

We noticed that the stretching and the degree of exposure are both controlled by the viscosity of the surrounding mantle. The stretching is a function of activation volume (see Fig. 11e), whereas the degree of exposure is mainly a function of the friction angle (see Fig. 11f). This is because these two phenomena occur under different conditions. The stretching occurs when the protocore is on the way to the planetary surface. The exposure, by contrast, happens when the protocore hits the planetary surface.

### 3.5. The completeness of core formation

Radial profiles of average and standard deviation in density (see second column and third column of Fig. 10) provide information on the chemical distribution and on its time evolution. Case B (test 64, fragmentation mode) has a distinct iron core and a clear core–mantle boundary (see green line in the second and third figure of second row). Other two modes (cases A, C, and D) have high density standard deviation inside the core region, because the iron core of each model is not located at the center of the protoplanet and is pushed aside by the remaining protocore (see the second column of Fig. 3, and the third column of Figs. 5 and 6). The core formation in these models is thus not entirely completed, but reaches an intermediate steady state due to the rigidity of the remaining protocore. The later can either deform slowly during the following thermal equilibration if no significant impacts on the planetary surface will occur, or be destroyed by impacts if planetary accretion will continue. Large chemical heterogeneity exists in the region from core–mantle boundary to surface in all models because of the leftover iron in the mantle. The standard deviation in density

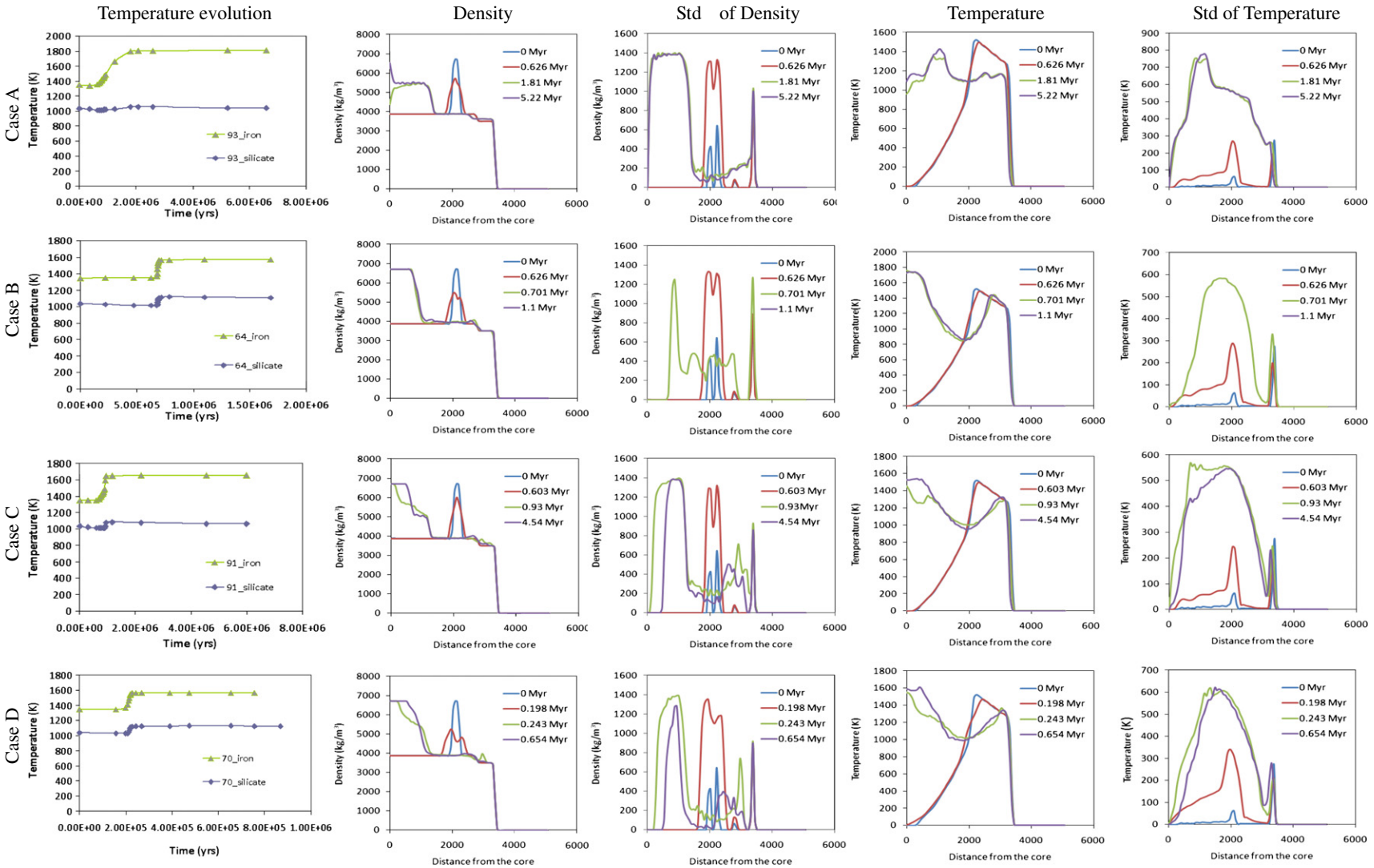


**Fig. 10.** Average temperature evolution of iron and silicate, density profile, standard deviation of density profile, temperature profile and standard deviation of temperature profile for four models (cases A–D). Four lines in the second to fifth figure for each model represents four points in time, the initiation of the model, the start and the end of the temperature jump in the iron, the equilibrium state of iron average temperature, and are chosen from the first figure.

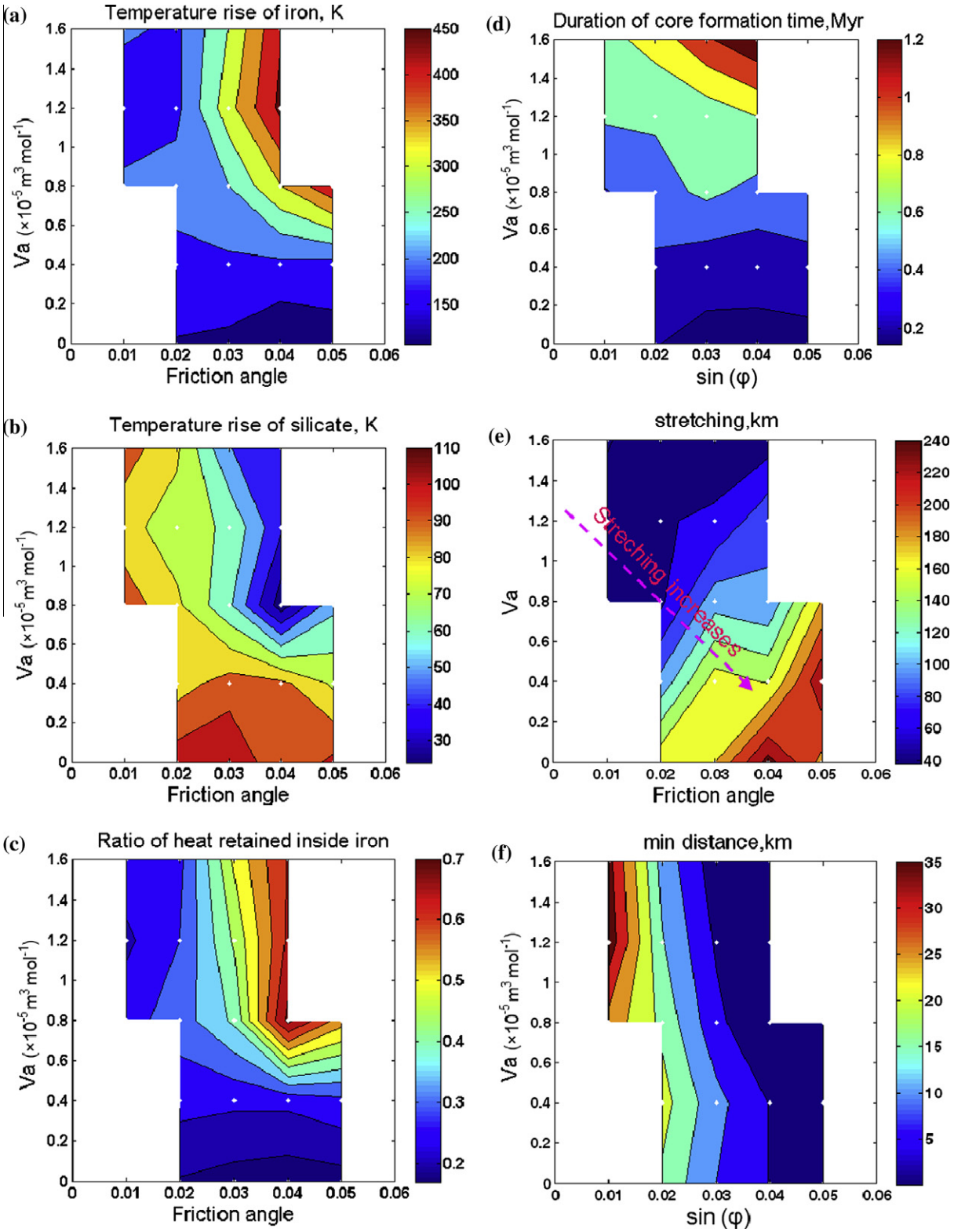


**Fig. 11.** Maps displaying observations from the models: (a) the temperature rise of iron. (b) The temperature rise of silicate. (c) Ratio of heat partition in iron. (d) The duration of metallic core formation corresponding to the moment when ~80% of metal is located in the central region of the planetary body. (e) The stretching distance and (f) the minimum distance of the protocore from the planetary surface.

can be high (up to 12% in fragmentation mode), but it will be reduced with time as the iron drops sink down further.

Radial profiles of average and standard deviation in temperature provide information on the thermal state at each stage of the core formation, including at the end of core formation (see fourth and fifth column of Fig. 10). Most of the models have a hot core with temperature around 1500–1800 K. The highest temperature can not be found in the planetary center in case A as the large remaining protocore still occupies a significant part of the central region (second column of Fig. 3). The average temperature

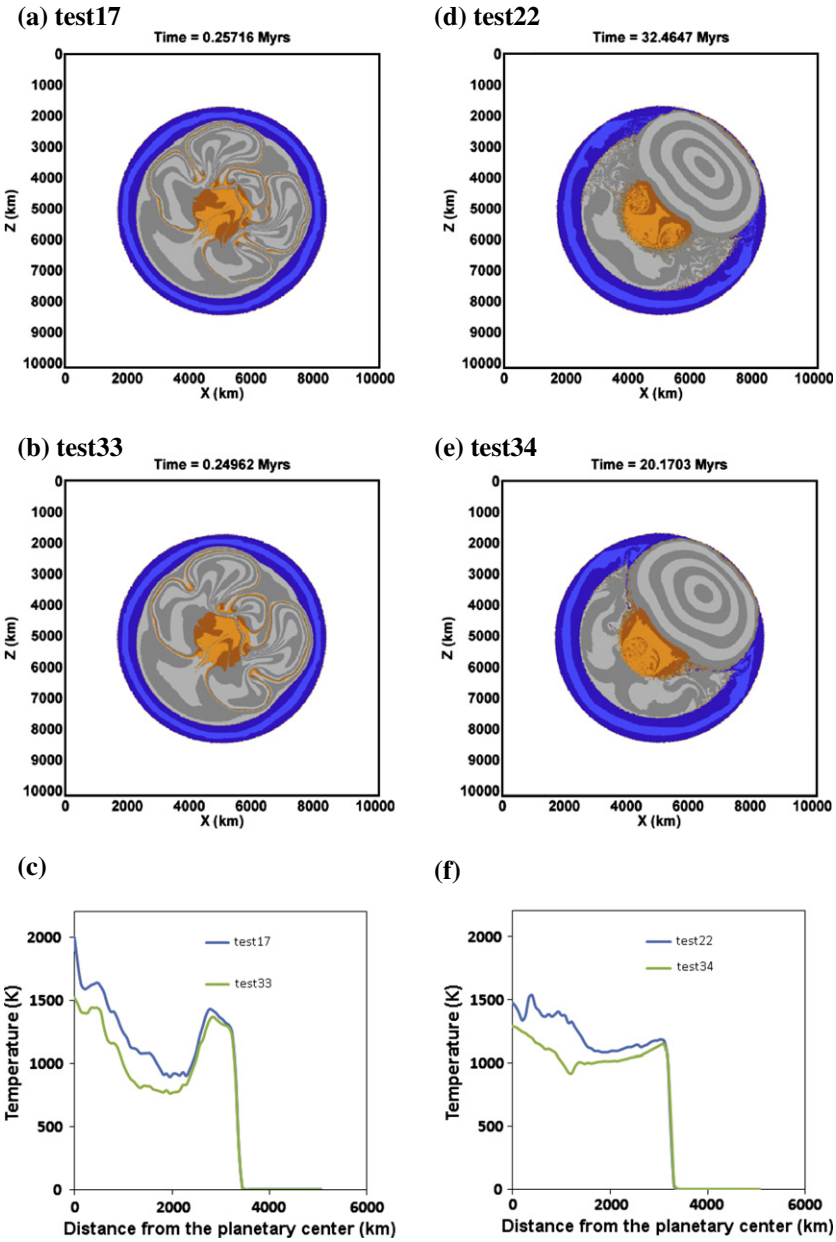


**Fig. 12.** Numerical results from two tests, (test 17 and test 22) showing the effect of shear heating on core formation. (a) and (b) are snapshots with similar chemical configuration from test 17 and test 33 (without shear heating contribution). (c) The comparison of temperature profiles for these two models. (c) and (d) are snapshots with similar chemical configuration from test 22 and test 34 (without shear heating contribution). (c) The comparison of temperature profiles for these two models.

in cases A, C and D keeps rising because with high temperature variation, the iron is slowly equilibrated, owing to the high viscosity applied in the model. The end of core formation visualized by our models does not in fact imply the end of planetary history of the embryo. The internal thermal and chemical structure could be deviated by subsequent events. In particular, such planetary embryos may further participate in chaotic impacts contributing to the growth of Earth-size planets.

## 4. Discussion

### 4.1. Deformation of the protocore

The core formation related to the cold accretion scenario is closely related to the destruction of the protocore, which can be understood by determining the dominant deformation type. Panels g and h in Fig. 3 and j–l in Figs. 4–6 show the dominant deformation type. We determined the type of deformation from the logarithm of the ratio between the ductile (viscous deformation) and brittle/plastic (brittle/plastic yielding) viscosities. When the value is above zero (i.e. the ratio is above one), brittle/plastic deformation is dominant, otherwise the deformation is largely ductile.

In our initial setup the protocore is divided by the iron layer into two distinct parts, the colder central region and the hotter outer protocore shell (Fig. 1). Our numerical experiments indicate that the cold central part of the protocore was dominated by brittle/plastic deformation, whereas the protocore shell and the outermost silicate mantle were in the ductile regime. As a result, the outskirt of the central part of the protocore can easily change its deformation mechanism from brittle/plastic to ductile regime

due to the change of pressure, stress and temperature, which are feedbacks from the ongoing core formation.

Variations of the rheological parameters like activation volume make the deformation of the outskirt of the protocore more difficult, and control the size of the remaining protocore and the reshaping mode of the core formation. The size of the region dominated by brittle/plastic deformation in the protocore is larger in case C (Fig. 5j) than in case D (Fig. 6j), suggesting that the activation volume (see test 1 in Fig. 7) prevent mechanical mixing between iron flow and surrounding silicate during core formation.

The deformation of the protocore, from spherical to elliptic shape (Fig. 13a), in the exposure mode is associated with the cross shape of the strain-rate fields that implies localized viscoplastic deformation along the conjugate planetary scale shear zones dividing the protocore. This localized viscoplastic deformation is triggered by high deviatoric stresses (reaching the brittle/plastic strength limit $\sigma_{yield}$ in some places) in the protocore that are maintained during the iron core formation. Similar cross-shape brittle/plastic strain localization is also observed for cases C (Fig. 5) and D (Figs. 6 and 13).

The fragmentation mode of core formation is associated with the sinking of secondary iron diapirs (case B, Fig. 4c). For this model the brittle/plastic rheology is weak enough, and the deviatoric stress exerted by the iron diapirs/ponds can yield the underlying plastically weak protocore in many locations (Fig. 13b). The results for the transition mode are more complicated, but the brittle/plastic strength of the primordial material and the exerted deviatoric stress on the protocore are still the main factors that control the reshaping of the protocore during the iron core formation (Fig. 13c). Like in the exposure mode, conjugate shear zones are initially formed by viscoplastic deformation inside the protocore. In the later stages, thermal feedback from shear heating increases temperature along shear zones that turns the deformation regime into viscous deformation. Due to the strong temperature dependence of viscosity, viscous deformation finally dominates the deformation of the protocore (Figs. 6 and 13c).

### 4.2. Timescale of core formation

We estimated the duration of the core formation as the time needed to accumulate ~80% of the iron from the original iron shell in the central region of the planetary embryo (Fig. 11d). According to this definition, core formation takes less than 2 million years in our study (Fig. 11d). For the strongest rheology (silicate-rich material does not significantly yield and behaves quasi viscous), the timescale is consistent with the results obtained for Newtonian rheology by Lin et al. (2009). The timescale is mainly controlled by the activation volume whereas, the friction angle plays only a role when the activation volume is large ($V_a = 1.2 \times 10^{-5}$ m$^3$ mol$^{-1}$) (Fig. 11d). Note that the upper-right corner in this panel is associated with a stiff, large protocore. This confirms results from previous studies with Newtonian rheology, which indicated that the duration of core formation rises with the protocore viscosity (Honda et al., 1993; Lin et al., 2009). In these cases the duration of the core formation for cold accretion is controlled by the destruction of the protocore. However, when the protocore is not strong enough (the activation volume and/or friction angle are low), the duration is mainly controlled by activation volume: the lower the activation volume, the smaller the remaining protocore. Furthermore, the protocore is more easily displaced from the center and replaced by iron.

In contrast to our study, Senshu et al. (2002) suggested much longer timescales (0.5–1 Gyr) of core formation. Their estimates for the timescale of core formation are derived from analytical model of Honda et al. (1993) based on isoviscous protocore assumption. For these estimates Senshu et al. used a high and uniform viscosity ($10^{24}$ Pa s) of the protocore that remains constant with time. In contrast, according to our models non-Newtonian rheology and energy feedback from shear heating create localized deformation of the embryo and dramatically reduce the timescale of core formation. Also, in our model the protocore rapidly deviates from the planetary center by degree 1 instability creating a direct pathway for iron to move into the center. This aspect is not taken into account in the analytical model of Honda et al. (1993).

### 4.3. Heat partition

Our model suggests an opposite observation compared to Samuel et al. (2010) regarding the heat partition between iron and silicates. This discrepancy results from dealing with different iron transport mechanisms. Samuel et al. (2010) work assumed iron diapirs, whereas in our models most of the iron is transported into the iron core through channel-like structures along the outer-face of the protocore. As suggested by Ke and Solomatov (2009) the diapir mechanism results in strong heat partitioning into the mantle, whereas the dyke or channel mechanism leads to a hot iron core as observed in our study (see also Golabek et al. (2009)).

The value of heat capacity of iron influences heat partition rather insignificantly. According to our test experiments lowering of iron heat capacity by the factor of two results in only ~5% decrease in the heat partitioning into the iron phase. Although temperature of iron in the regions of intense shear heating rises more significantly in case of decreased heat capacity total amount of heat partitioned into this phase remains almost constant.

### 4.4. Model limitations

#### 4.4.1. Technical limitations

Our model has technical limitations when dealing with the gravitational field. The first is the enforced uniform gravitational potential boundary condition at a certain distance from the planetary body's center, which may lead to artificial deformation inside the body. The second limitation is to model a 3D gravitational potential in 2D geometry in a simplified manner. It can result in an overestimation of the gravitational acceleration outside of the planetary body (Lin et al., 2009).

In order to test dependency of numerical results from grid resolution we repeated calculations with an increased grid resolution of 513 × 513 points (instead of 150 × 150 points) for five selected cases (A–E). The general characteristics of the discussed core formation modes do not change with the higher resolution. For instance, temperature profiles at the same thermal stage for models case A (test 93) and case B (test 64) are similar with the two grid resolutions (Fig. 14a and b). With larger resolution more small iron diapirs can be created near the protocore. but again, it does not change entire chemical distribution significantly (see Fig. 14c and d). The difference between the different modes regarding the exposure, the duration of the core formation and the ratio of heat retained in iron do not change when the resolution is increased, and they follow a similar trend (see Fig. 14e, f and g). Higher resolution can resolve more deformation in the silicate mantle and results in lower heat retained in iron. The phenomena we observed in the main experiments are therefore robust.

Fig. 15a and b shows the influence of the viscosity of the weak layer surrounding the planetary body on the exposure, and the duration of core formation for two modes of deformation (case A for exposure mode, and case B for fragmentation mode). When the viscosity is lower than $10^{17}$ Pa s, the viscosity contrast between weak layer and planetary surface increases to ≧100–1000, and the influence of the weak layer is negligible. The aspherical deviation of the planetary embryo and the exposure of the protocore, which are the characteristics for core formation by the protocore destabi-

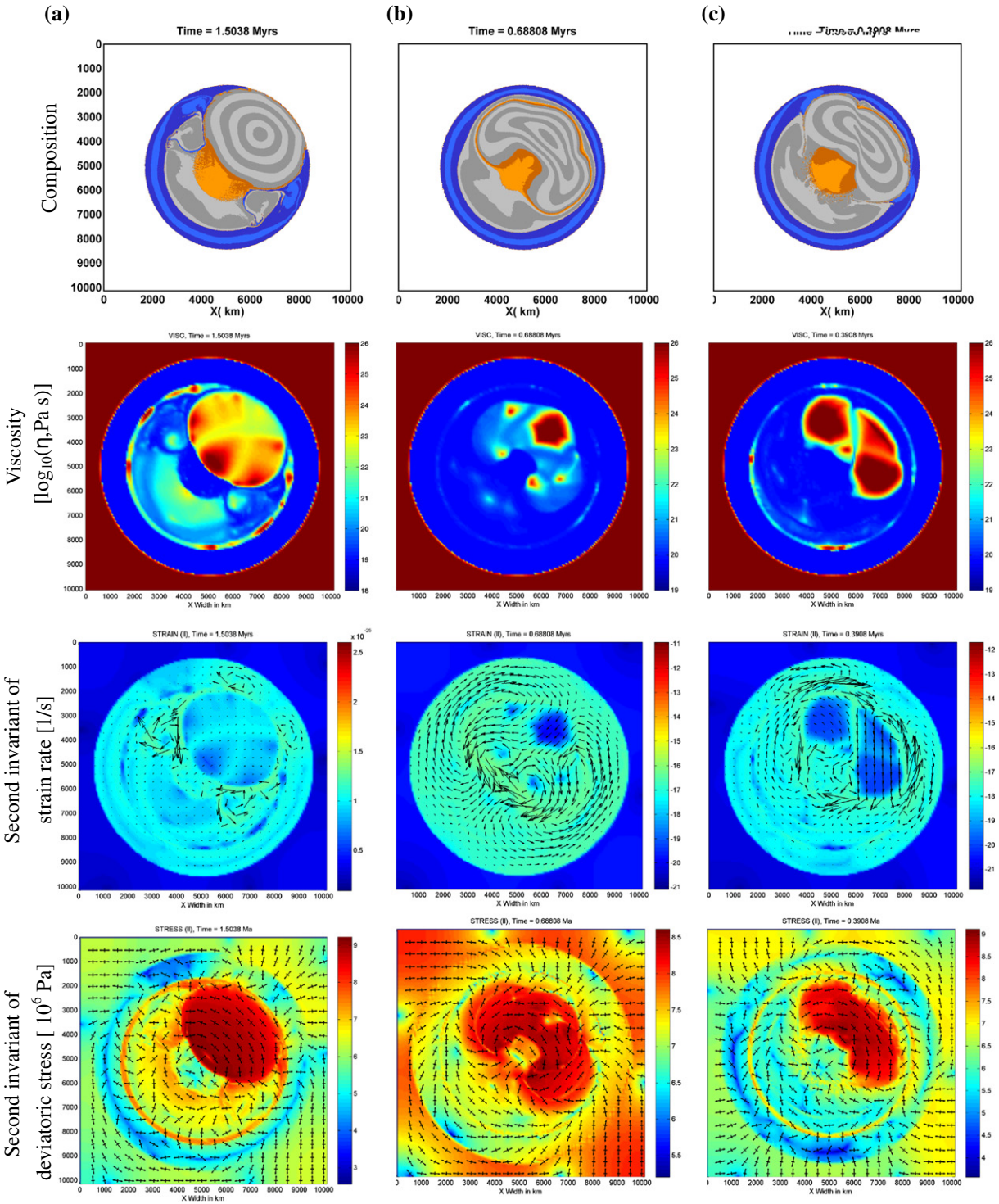


**Fig. 13.** Additional fields (viscosity, second invariant of strain rate with velocity (black arrows), and second invariant of the deviatoric stress with stress principal axis orientation (elongated crosses, long and short branches of the crosses show extension and shortening directions)) for three models displaying three different core formation modes (cases A, B, and D) are displayed. Column A displays the fields for the last stage of case A. Column B shows the second stage of case B, whereas column C shows the last stage of case D.

lization, still exist. However, the level of these phenomena decreases when using a more realistic free surface.

The benchmarks of dealing with large viscosity variations observed in silicate (Fig. 3g and h) have been addressed and discussed in Gerya and Yuen (2003, 2007) and Gerya (2010) including numerical code examples (Gerya, 2010). In this respect, our model is numerically stable and accurate. However, in some regions, iron and even silicate might be partially or fully molten and have very low liquid viscosities that are not taken into account in our model. In these regions multiphase flow approaches (e.g., Ricard et al., 2009) treating coupled deformation of solid matrix and percolation of melts can be more appropriate for the accurate numerical treatment.

### 4.4.2. Conceptual limitations

Our model applied the Mohr–Coulomb yielding criterion to higher confining pressures. It was experimentally verified only

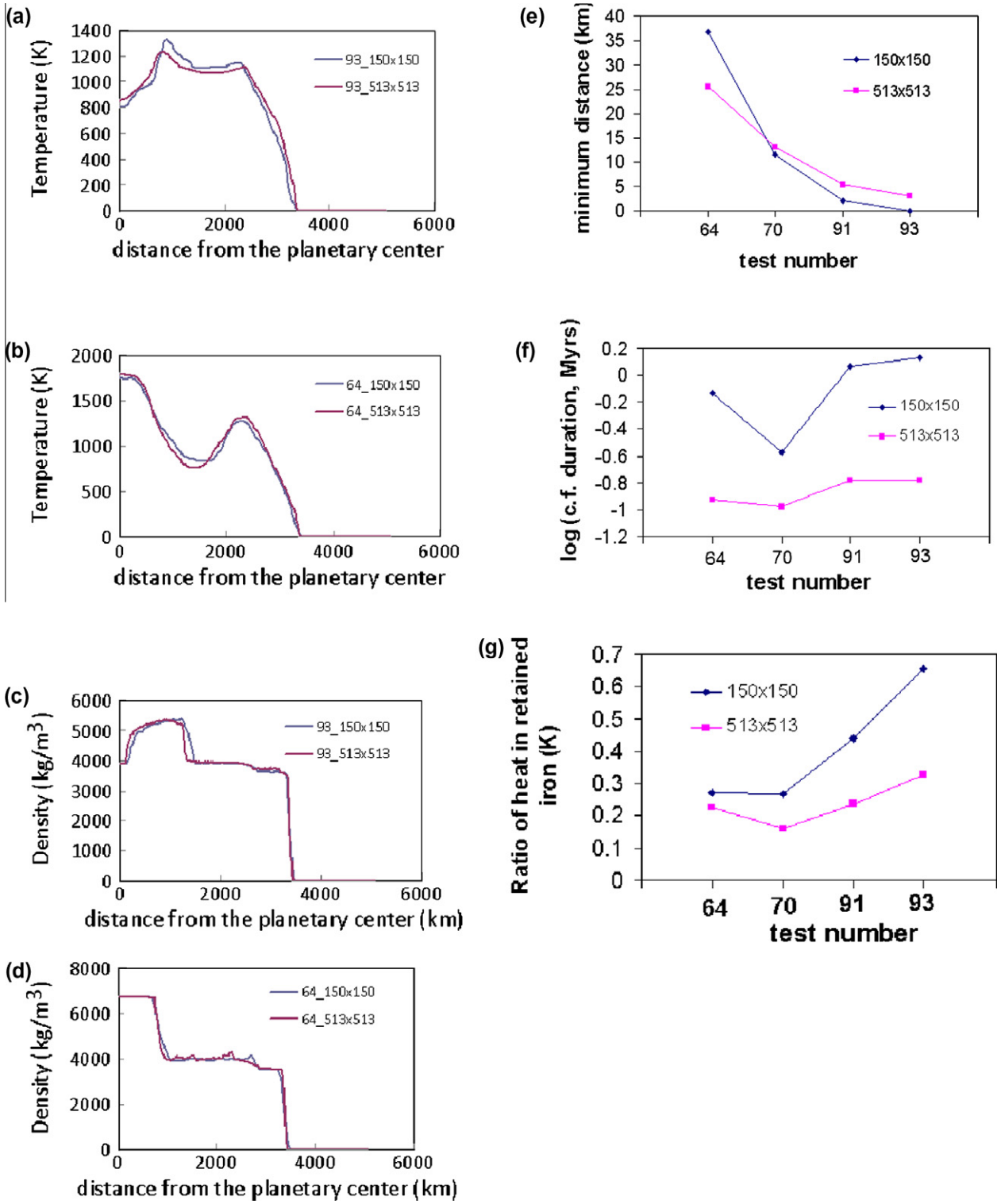


**Fig. 14.** Numerical results of two models, case A (test 93), and case B (test 64), to show the effect of grid resolution. (a) Displays the temperature profiles for low and high resolution of case A (test 93) with similar chemical distribution. (b) Displays the temperature profiles for low and high resolution of case B (test 64) with similar chemical distribution. (c) Displays the density profiles for low and high resolution of case A (test 93) with similar chemical distribution. (d) Displays the density profiles for low and high resolution of case B (test 64) with similar chemical distribution. (e) Shows the minimum distance of the protocore from the planetary surface for low and high resolution from four models, cases A–D (test 93, test 64, test 91, test 70). (f) Shows the duration of core formation for low and high resolution from four models, cases A–D (test 93, test 64, test 91, test 70). (g) Shows the ratio of heat retained in iron for low and high resolution from four models, cases A–D (test 93, test 64, test 91, test 70).

for confining pressures up to a few hundreds of MPa (Ranalli, 1995), but its validity at larger pressure should be checked. The strength of the material could become less sensitive to temperature and pressure at relatively low temperature and/or high stress condition (Karato, 2008), which is a characteristic of the protocore in the cold accretion scenario.

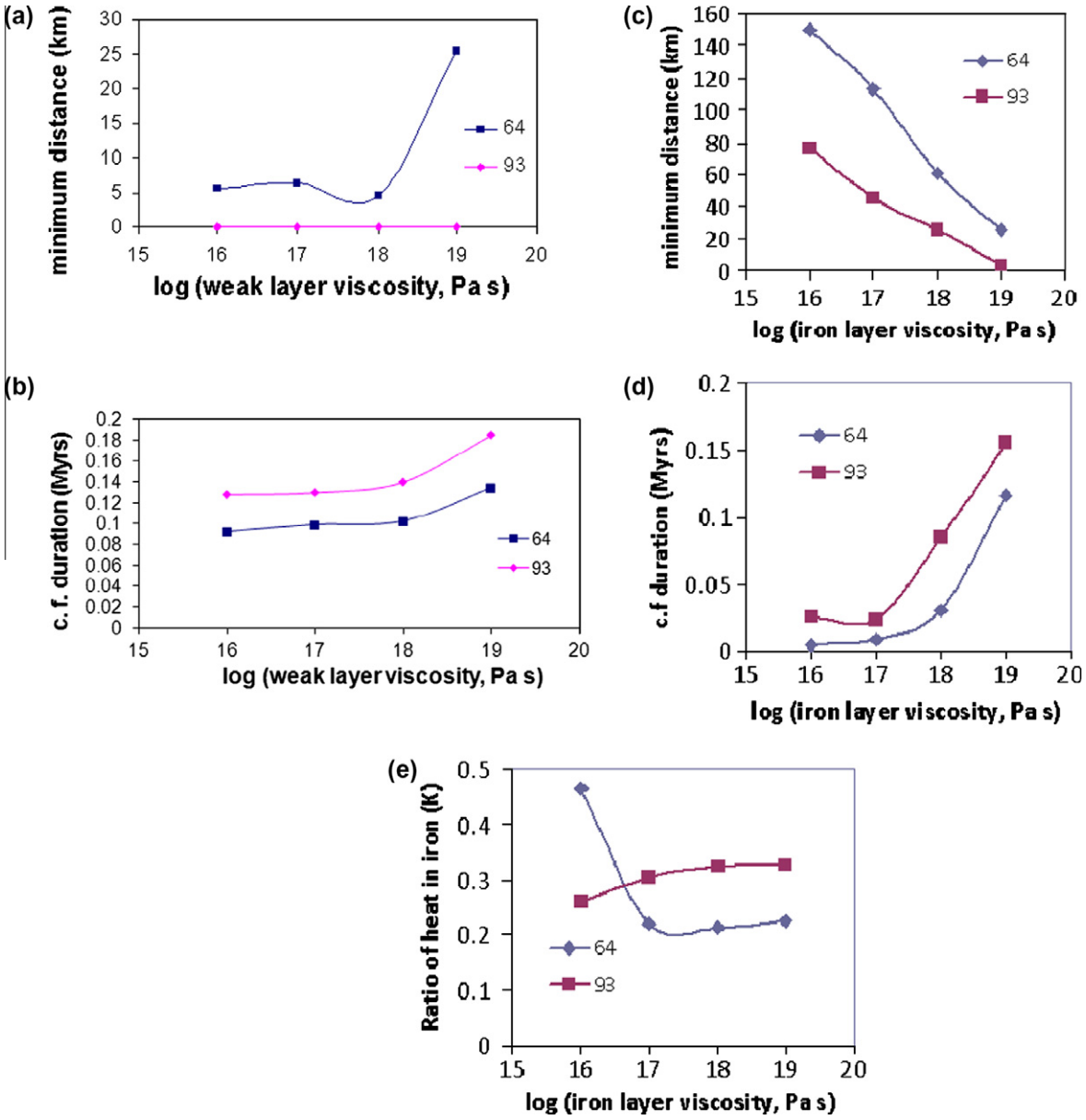


**Fig. 15.** Numerical results of two tests, case A (test 93), and case B (test 64) are shown to emphasize the effects of the weak layer viscosity and the iron viscosity. (a) The minimum distance of the protocore from the planetary surface depending on the weak layer viscosity. (b) The duration of core formation depending on the weak layer viscosity. (c) The influence of the iron viscosity on the minimum distance of the protocore from the planetary surface. (d) The influence of the iron viscosity on the duration of core formation. (e) The influence of the iron viscosity on the ratio of heat retained in iron.

The influence of iron-layer viscosity is shown in Fig. 15c–e. When the iron-rich layer viscosity is higher, the level of the protocore exposure is enhanced because the strong iron pushes away the protocore more from the planetary center. On the contrary when the iron-rich layer viscosity is lower, the iron flow can be easier to accumulate to the center without much deviation of the protocore and intrude the protocore directly, which results in a shorter duration of core formation (Fig. 15d). The transition mode and fragmentation mode are favored by lower iron viscosity and the strength of the protocore is still the main factor that controls the reshaping mode and heat distribution (Fig. 15e). However, the amount and size of secondary diapirs could cause deviation on heat partition on iron/silicate as case B (test 64) in Fig. 15e. Fewer and bigger secondary diapirs observed in iron viscosity $10^{16}$ Pa s elevates heat ratio retained in iron. Further modifications to heat partitioning between iron and silicate can be expected to come from melting processes that should potentially take place in the hotter zones of the embryo (e.g., Ricard et al., 2009).

Another conceptual limitation of our model is that it uses thermal and compositional structure for the final stage of accretion scenario investigated by Senshu et al. (2002). In fact, planetary scale instability may start earlier in the history of the accreting embryo. Nevertheless, test runs starting from earlier stages of the accretion model of Senshu et al. (2002) containing thinner iron layer produce the same general trends of the evolution of the embryo.

## 5. Conclusion

We investigated the rheological and thermal effects on core formation by gravitationally destabilizing an iron shell in the interior

of the planetary embryo, as suggested by previous models on cold accretion (Sasaki and Nakazawa, 1986; Honda et al., 1993; Karato and Murthy, 1997; Senshu et al., 2002). In these experiments, we observed three main modes of deformation, the exposure, the fragmentation, and the transition mode, are observed in our experiments. In the exposure mode, a dichotomy is created on the surface and maintained in one hemisphere of the planetary embryo until the end of the simulation. In the fragmentation mode, the protocore dislocates into distinct fragments that are redistributed around the newly formed iron core, as the proposed by Stevenson (1981). Several models belonging to the transition mode are characterized by development of planetary-scale rupture zones, which may cause mega-quakes during the core formation if the stress is released in a short period of time. The core formation for the cold accretion scenario is closely related to the destruction of the protocore. The rheology of silicates controls the reshaping mode of cold formation, and the secondary iron diapirs provide additional deviatoric stress to deform the protocore by descending iron drops or cross-shape stain localization, which may lead to shear zone. The exposure of the protocore and aspherical deviation of the planetary shape are observed in our study, as well as in the Newtonian rheology. The former is characterized by a strong protocore (with high friction angle), whereas the latter is characterized by a strong (but small) protocore with high friction angle and low activation volume. The duration of core formation is mainly controlled by the activation volume. A large fraction of heat can partition into the iron when the protocore is strong and large (i.e., for high friction angle and high activation volume). These observations do not depend on the grid resolution and may happen during core formation on planetary bodies with a cold accretion pre-history. Our models show that the strain localization from brittle–ductile rheology has crucial influences on core formation mechanism. However, the feedback from shear heating has been limited to certain areas, which plays only a negligible role on the mode of core formation in the case of cold accretion.

## Acknowledgements

We express our gratitude to Frédéric Deschamps for valuable discussions and anonymous reviewers for helpful comments. This work was supported by ETH grant TH-2207-1 to GJG, and CMG program of NSF to DAY.

## Reference

Baker, J., Bizzarro, M., Wittig, N., Connelly, J., Haack, H., 2005. Early planetesimal melting from an age of 4.5662 Gyr for differentiated meteorites. Nature 436, 1127–1131.

Chambers, J.E., Wetherill, G.W., 1998. Making the terrestrial planets: N-body integrations of planetary embryos in three dimensions. Icarus 136, 304–327. doi:10.1006/icar.1998.6007.

Chambers, J.E., Wetherill, G.W., 2001. Planets in the asteroid belt. Meteorit. Planet. Sci. 36, 381–399.

Day, J.M.D., Ash, R.D., Liu, Y., Bellucci, J.J., Rumble III, D., McDonough, W.F., Walker, R.J., Taylor, L.A., 2009. Early formation of evolved asteroidal crust. Nature 457, 179–182.

Elsasser, W.M., 1963. Early history of the Earth. In: Geiss, J., Goldberg, E. (Eds.), Earth Science and Meteorites. North Holland, Amsterdam, pp. 1–30.

Gerya, T.V., 2010. Introduction to Numerical Geodynamic Modelling. Cambridge University Press, Cambridge. pp. 241–267.

Gerya, T.V., Yuen, D.A., 2003. Characteristics-based marker-in-cell method with conservative finite-differences schemes for modeling geological flows with strongly variable transport properties. Phys. Earth Planet. Inter. 140 (4), 293–318.

Gerya, T.V., Yuen, D.A., 2007. Robust characteristics method for modeling multiphase visco-elasto-plastic thermo-mechanical problems. Phys. Earth Planet. Inter.. doi:10.1016/j.pepi.2007.04.015.

Golabek, G.J., Schmeling, H., Tackley, P.J., 2008. Earth's core formation aided by flow channelling instabilities induced by iron diapirs. Earth Planet Sci. Lett. 271, 24–33.

Golabek, G.J., Gerya, T.V., Kaus, B.J.P., Ziethe, R., Tackley, P.J., 2009. Rheological controls on the terrestrial core formation mechanism. Geochem. Geophys. Geosyst. 10, Q11007. doi:10.1029/2009GC002552.

Greenwood, R.C., Franchi, I.A., Jambon, A., Buchanan, P.C., 2005. Widespread magma oceans on asteroid bodies in the early Solar System. Nature 435, 916–918.

Grimm, R.E., McSween, H.Y., 1993. Heliocentric zoning of the asteroid belt by aluminum-26 heating. Science 259, 653–655.

Hevey, P.J., Sanders, I.S., 2006. A model for planetesimal meltdown by $^{26}$Al and its implications for meteorite parent bodies. Meteorit. Planet. Sci. 41, 95–106.

Honda, R., Mizutani, H., Yamamoto, T., 1993. Numerical simulation of Earth's core formation. J. Geophys. Res. 98, 2075–2089.

Ichikawa, H., Labrosse, S., Kurita, K., 2010. Direct numerical simulation of an iron rain in the magma ocean. J. Geophys. Res. 115, B01404. doi:10.1029/2009JB006427.

Ida, S., Nakagawa, Y., Nakazawa, K., 1987. The Earth's core formation due to Rayleigh–Taylor instability. Icarus 69, 239–248.

Ida, S., Nakagawa, Y., Nakazawa, K., 1989. The Rayleigh-Taylor instability in a self-gravitating two-layer fluid sphere. Earth Moon Planets 44, 149–174.

Kameyama, M., Yuen, D.A., Karato, S., 1999. Thermal–mechanical effects of low-temperature plasticity (the Peierls mechanism) on the deformation of a viscoelastic shear zone. Earth Planet. Sci. Lett. 168, 159–172.

Karato, S., 2008. Deformation of Earth Materials. Cambridge University Press, New York. pp. 120–121.

Karato, S., Murthy, V.R., 1997. Core formation and chemical equilibrium in the Earth – I. Physical considerations. Phys. Earth Planet. Inter. 100, 61–79.

Ke, Y., Solomatov, V.S., 2009. Coupled core–mantle thermal evolution of early Mars. J. Geophys. Res. 114, E07004.

Lin, J.R., Gerya, T.V., Tackley, P.J., Yuen, D.A., Golabek, G.J., 2009. Numerical modeling of protocore destabilization during planetary accretion: Methodology and results. Icarus. 204, 732–748.

Melosh, H.J., 1990. Giant impacts and the thermal state of the early Earth. In: Newsom, H.E., Jones, J.H. (Eds.), Origin of the Earth. Oxford University Press, New York, pp. 69–83.

O'Brien, D.P., Morbidelli, A., Bottke, W.F., 2007. The primordial excitation and clearing of the asteroid belt—Revisited. Icarus 191, 434–452.

Ranalli, G., 1995. Rheology of the Earth, second ed. Chapman and Hall, London. pp. 101–102.

Ricard, Y., Šrámek, O., Dubuffet, F., 2009. A multi-phase model of runaway core–mantle segregation in planetary embryos. Earth Planet. Sci. Lett. 284, 144–150.

Rubie, D.C., Nimmo, F., Melosh, H.J., 2007. Formation of Earth's core. In: Schubert, G., Stevenson, D.J. (Eds.), Treatise on Geophysics, vol. 9. Elsevier, New York, pp. 51–90.

Sahijpal, S., Soni, P., Gupta, G., 2007. Numerical simulations of the differentiation of accreting planetesimals with $^{26}$Al and $^{60}$Fe as the heat sources. Meteorit. Planet. Sci. 42, 1529–1548.

Samuel, H., Tackley, P.J., 2008. Dynamics of core formation and equilibration by negative diapirism. Geochem. Geophys. Geosyst. 9, Q06011. doi:10.1029/2007GC001896.

Samuel, H., Tackley, P.J., Evonuk, M., 2010. Heat partitioning in terrestrial planets during core formation by negative diapirism. Earth Planet. Sci. Lett. 290, 13–19.

Sasaki, S., Nakazawa, K., 1986. Metal-silicate fractionation in the growing Earth: Energy source for the terrestrial magma ocean. J. Geophys. Res. 91, 9231–9238.

Schmeling, H. et al., 2008. A benchmark comparison of spontaneous subduction models- Towards a free surface. Phys. Earth Planet. Interiors. 7, 8–9. doi:10.1016/j.pepi.2008.06.028.

Senshu, H., Kuramoto, K., Matsui, T., 2002. Thermal evolution of a growing Mars. J. Geophys. Res. 107 (E12), 5118. doi:10.1029/2001JE001819.

Stevenson, D.J., 1981. Models of the Earth's core. Science 214, 611–619.

Stevenson, D.J., 1990. Fluid dynamics of core formation. In: Newsom, H.E., Jones, J.H. (Eds.), Origin of the Earth. Oxford University Press, pp. 231–249.

Wetherill, G.W., 1992. An alternative model for the formation of the asteroids. Icarus 100, 307–325.

Zhong, S.J., Parmentier, E.M., Zuber, M.T., 2000. On the dynamic origin of asymmetric distribution of mare basalts. Earth Planet. Sci. Lett. 177, 131–140.